




Electrostatic interference control of a high-energy coherent electron beam using three-element Boersch phase shifters

Pooja Thakkar^{1,2*}, Vitaliy A. Guzenko³, Peng-Han Lu⁴, Rafal E. Dunin-Borkowski^{4,5}, Jan Pieter Abrahams^{1,2,6}, and Soichiro Tsujino^{1,2*} 

¹Division of Biology and Chemistry, Paul Scherrer Institut, Forschungsstrasse 111, 5232 Villigen PSI, Switzerland

²Swiss Nanoscience Institute, University of Basel, Klingelbergstrasse 82, 4056 Basel, Switzerland

³Photon Science Division, Paul Scherrer Institut, Forschungsstrasse 111, 5232 Villigen PSI, Switzerland

⁴Ernst Ruska-Centre for Microscopy and Spectroscopy with Electrons and Peter Grünberg Institute, Forschungszentrum Jülich, Wilhelm-Johnen-Strasse, 52425 Jülich, Germany

⁵Aachen University, Ahornstraße 55, 52074 Aachen, Germany

⁶University of Basel, Klingelbergstrasse 70, 4056 Basel, Switzerland

*E-mail: pooja.ummethala@gmail.com; soichiro.tsujino@psi.ch

Received July 11, 2024; accepted August 23, 2024; published online October 22, 2024

Static phase shifters have been intensely studied for generating two- and three-dimensional electron beam patterns. However, those are restricted to specific electron beam energies and microscope settings. Aiming at overcoming such limitations, the development of programmable phase shifters based on e.g. a Boersch phase is an active field of research. We recently demonstrated a three-element Boersch phase shifter device [Thakkar et al., *J. Appl. Phys.* **128**, 134502 (2020)], which was fabricated by electron beam lithography and is compatible with up-scaling. However, it suffers from parasitic beam deflection and cross-talk. Here, we report a five-layer phase shifter device, which is based on a metal–insulator–metal–insulator–metal structure as originally envisioned by Boersch that reduces cross-talk. We demonstrate a three-element Boersch phase shifter that shows minimal beam deflection of voltage-controlled three-electron-beam interference patterns in a transmission electron microscope operated at 200 keV. The feasibility of using such multi-element phase shifter arrays is discussed in this article.

© 2024 The Japan Society of Applied Physics. All rights, including for text and data mining, AI training, and similar technologies, are reserved.

1. Introduction

Control of the phase of an electron wavefront for electron beam shaping is an active area of research for producing arbitrary two- and three-dimensional electron beam patterns.^{1–3} Holographic phase plates have been used to produce vortex beams^{4–7} and advanced Bessel beams^{8–10} for spectroscopy and beam propagation control. In order to further exploit this methodology, programmable pixelated phase shifter arrays are needed, which can be used to tune the beam shape to a target sample or for different electron beam energies and microscope settings, as is common in light optics.¹¹ Such flexibility would have a significant impact on electron wavefront engineering applications.^{12–16} As a result of the importance of phase distributions for image formation, a programmable device would also be useful for phase contrast imaging,¹⁷ lens-less imaging and holographic image recovery^{18–20} beyond the use of Zernike phase contrast imaging with static phase plates.^{21–27} A programmable phase shifter would also be instrumental for the realization of single-pixel electron-beam imaging,^{28–30} which offers possibilities for novel spectroscopic imaging by using an advanced beam analyzer for energy and momentum. There has recently been tremendous progress in the ultrafast modulation of electron wave packets by laser pulses.^{31–37} In contrast, one of the development aims for programmable phase shifter arrays is their integration into state-of-the-art high-resolution electron microscopes without the need for ultrafast modulation of the electron beam or energy filtering.³⁵

A Boersch phase shifter device^{24–27,38–40} is one of the candidates for a phase shifter technology. It was originally proposed to realize Zernike phase contrast imaging¹⁷ in electron microscopy, and relies on the fact that an electron wave experiences a phase shift when it propagates through an

aperture, to which a small electrostatic potential is applied. Although single-element Boersch phase shifters have been tested,^{24–27,38} their fabrication has relied on focused-ion-beam (FIB) milling of stacks of metal and insulator layers. Recently, a four-element phase shifter was reported.¹⁴ However, FIB milling is likely to face difficulties in the fabrication of larger phase shifter arrays, in part because of redeposition.⁴¹

We recently studied a three-element Boersch phase shifter device, which was fabricated using electron beam lithography with CMOS-compatible processing.¹⁶ We were able to control three-electron-beam interference by applying a few Volts of bias to individual Boersch elements for a 200 keV coherent electron beam.¹⁶ However, as a result of the fact that the simplified three-layer design was based on a metal–insulator–metal structure, the use of unscreened contact wires to the phase shifter elements caused parasitic deflection of the electron beam. This deflection should be eliminated since cross-talk is difficult to compensate for a larger array of phase shifters.

The purpose of the present study is to realize a three-element Boersch phase shifter device, in which a top shielding electrode is introduced to prevent parasitic deflection of a far-field electron interference pattern. In Sect. 2, we describe the design of the device and the fabrication methods. In Sect. 3, we describe the results of the experimental characterization of the fabricated device. Finally in Sect. 4, we summarise and conclude the work.

2. Device design and fabrication method

2.1. Design consideration of Boersch phase shifter device

We first investigate the structural parameters for the fabrication of a Boersch phase shifter with a metal–insulator–metal–insulator–metal (MIMIM) five-layer structure. We show electrostatic simulations of a phase shifter element, extend

© 2024 The Japan Society of Applied Physics. All rights, including for text and data mining, AI training, and similar technologies, are reserved.

the fabrication procedure from an MIM to an MIMIM structure, and test the device in a high-energy transmission electron microscope (TEM).⁴²⁾

Figures 1(a) and 1(b) show a schematic cross-section and perspective view, respectively, of a Boersch phase shifter with an MIMIM structure. Figures 1(c) and 1(d) show scanning electron microscopy (SEM) images of a device, in which three metal layers are visible. When it is illuminated by a coherent electron beam, the three transmitted beams form a hexagonal interference pattern in the far-field. When the three beams have equal phases, the far-field pattern has a bright central spot. When the phase of one of the beams is shifted by applying a voltage, the interference pattern changes and its center becomes dark when the voltage corresponds to a π -phase shift. The phase shift is approximately proportional to the length of the potential distribution in the direction of the electron beam propagation and is theoretically constant across the aperture independent of the radius of the aperture.⁴⁰⁾ In the MIM structure device reported in Ref. 16, the phase shift was approximately $1.1\pi \text{ rad V}^{-1}$. However, as a result of the use of unshielded contact wires (CWs) to the phase shifter elements, the beam was also deflected by $\sim 0.35 \mu\text{mrad V}^{-1}$.

In order to study the impact of a top electrode on the shielding of the CWs in a MIMIM device, we conducted a finite element simulation. We first simulated the potential distribution around phase shifters without CWs. Figures 2(a)–2(c) show simulations for $dR_{TE} = 0.1 \mu\text{m}$ and $V_1 = 1 \text{ V}$, $V_2 = V_3 = 0 \text{ V}$, where dR_{TE} is the difference between the inner diameters of the top and bottom electrodes [see the inset to Fig. 2(b)] and V_n ($n = 1, 2, 3$) are voltages applied to the n th phase shifter. See the schematic with top and cross-section view in Fig. 3 for the detailed definition of the device parameters which are taken in to consideration for the simulation of five-layer three-element Boersch phase shifter device. The insulator 1 is the membrane substrate on which the device is fabricated and the Insulator 2 is the layer electrically separating the central layer (ring electrodes) from the top electrode layer. As the MIMIM device is an extension of the MIM device previously reported, the device dimensions of the bottom layer and the central layer are retained, and only the inner radius of the top metal layer is varied to understand its effects on the potential profile through

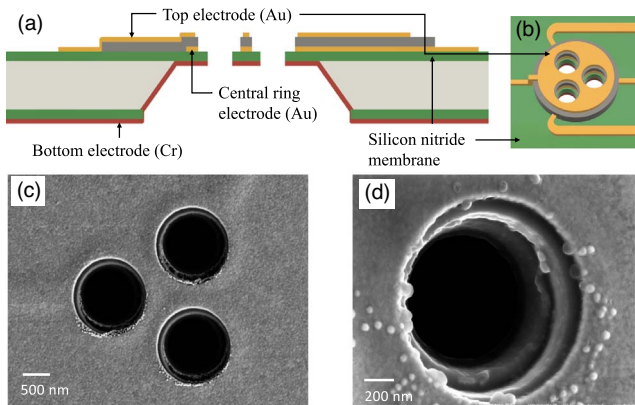


Fig. 1. Schematic (a) cross-section and (b) 3D perspective view of a five-layer Boersch phase shifter device with three elements, three contact wires, and a contact wire for grounding the top metal layer. (c) SEM image of three Boersch phase shifter elements. (d) High magnification SEM image of the sidewall of one element imaged at an angle of 20° .

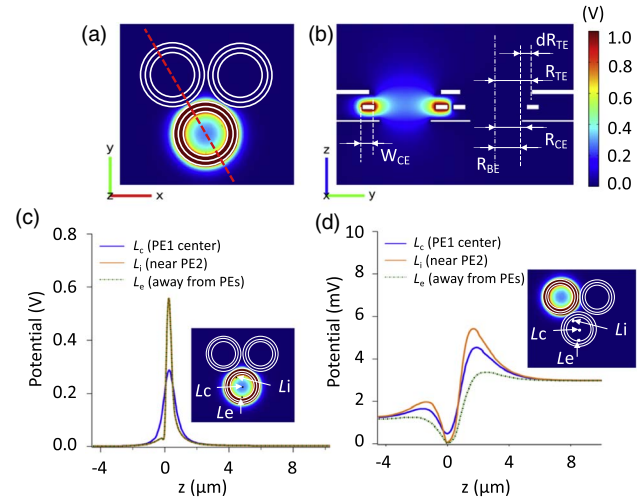


Fig. 2. Calculated 3D electrostatic potential of a three-element Boersch phase shifter elements (PE1, PE2 and PE3) (MIMIM). The contact wires to the ring electrode are omitted for simplicity. The center-to-center distance between the phase elements is $1.8 \mu\text{m}$. The radius of the apertures increases from the bottom to the top. We set $R_{BE} = 0.50 \mu\text{m}$, $R_{CE} = 0.60 \mu\text{m}$, and $W_{RE} = 0.25 \mu\text{m}$ for the aperture radii of the bottom and ring electrodes and the width of the ring electrode, respectively [Ref. 16]. The inner radius of the top electrode aperture R_{TE} is equal to $R_{BE} + dR_{TE}$. Here, $dR_{TE} = 0.2 \mu\text{m}$. PE1 is biased at 1 V , while PE2 and PE3 are at 0 V . The common top and bottom electrodes are at 0 V . (a) Cross-section of the $z = 0.5 \mu\text{m}$ plane. (b) Cross-section of a y - z plane through the dashed line in (a). (c) Potential distributions along lines parallel to the z -axis at L_c (center of PE1), L_i (close to PE2), and L_e (away from PE2 and PE3) inside PE1. (d) As for (c), but with PE2 biased at 1 V and PE1 and PE3 at 0 V , showing little cross-talk between neighboring phase shifters.

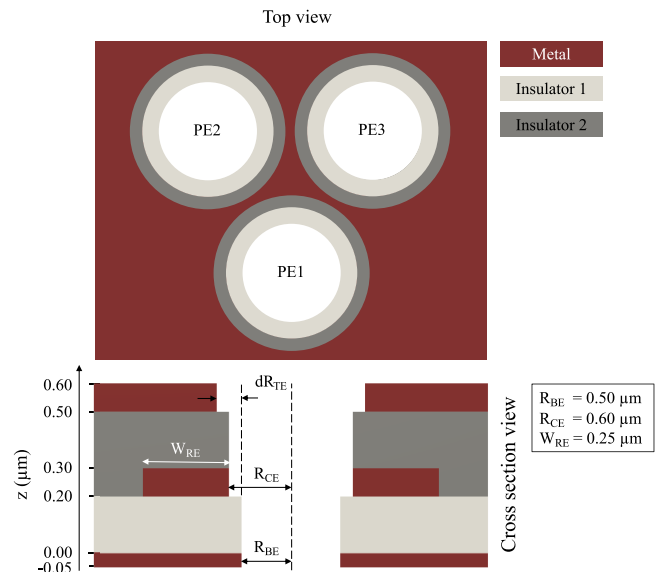


Fig. 3. Top view (top) and cross-section (bottom) view of the three-element Boersch phase shifter with five-layer, MIMIM structure. The contact wires to the ring electrode are omitted for simplicity.

the phase shifter element and also crosstalk. This is shown in Figure 4.

Figures 2(a) and 2(b) show that the potential is confined to the space between the top and bottom electrodes of the phase shifter, as is also apparent in Figs 4(a) and 4(b) from the potential profile $U_V(x, y, z)$ in the beam direction (the z -direction) and the phase shift ϕ_V for different values of dR_{TE} when the voltage is 1 V . The value of ϕ_V at position (x, y) is given by integration of $U_V(x, y, z)$ along the electron path. © 2024 The Japan Society of Applied Physics. All rights, including for text and data mining, AI training, and similar technologies, are reserved.

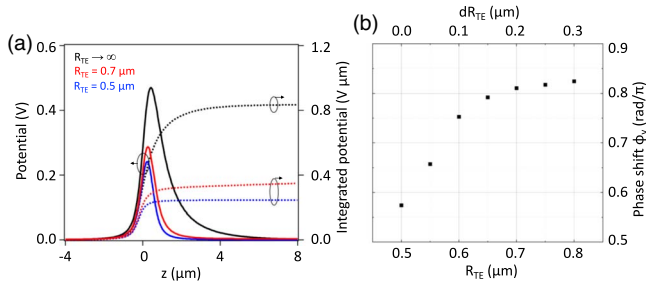


Fig. 4. (a) Potential along the z -direction through the center of a PE for $dR_{TE} = 0, 0.2 \mu\text{m}$ and ∞ . The right axis shows the z -integrated potential. (b) Relationship between phase shift per unit for a 200 keV electron beam energy.

trajectory (the z -direction), according to the expression

$$\phi_V(x, y) = \sigma \int_{-\infty}^{\infty} dz U_V(x, y, z), \quad (1)$$

where $\sigma = 7.29 \times 10^6 \text{ rad}/(\text{Vm})$ for a 200 keV electron beam.^{16,43} Although Eq. 1 is a function of (x, y) , ϕ_V is approximately constant across an aperture.⁴⁰ Figure 4(a) summarises the results of simulation for varying inner radius for top electrode. To understand the effect of dR_{TE} on the potential profile along the center of the electrode for an applied voltage of 1V, we consider three different cases as shown in the graph. For the case of three-layer (MIM) device, where R_{TE} can be considered to be of infinite value, the integrated potential is higher as it extends well above the central electrode but would also result in higher crosstalk. On the other hand the device design with $dR_{TE} = 0 \mu\text{m}$ or $R_{TE} = R_{BE}$ would be an ideal case for minimal crosstalk. Figure 4(b) shows that, when compared to the infinite value of dR_{TE} for the MIM case, the smaller values of dR_{TE} for a screened ring electrode decreases the phase shift, ϕ_V by reducing the extension of the potential above the aperture. For a more realistic and reproducible fabrication with electron beam lithography, we chose a value of $dR_{TE} = 0.2 \mu\text{m}$, for which the calculated crosstalk is below 2.7%. The dielectric constants of insulator 1 and insulator 2 considered for the simulation of our device, are equal to 7.5 and 3.8, respectively. The thicknesses of both insulators are equal to $0.2 \mu\text{m}$. The insulator 1 lies above $z = 0 \mu\text{m}$ as shown in the cross-section view in Figure 3.

In order to evaluate the effectiveness of shielding by the top electrode, we simulated the electrostatic field of a single phase element connected with a contact wire (CW) for $dR_{TE} = 0.2 \mu\text{m}$. We then determined the transverse deflection angle η_s from the electric field along the CW. η_s is given by the ratio, u_y/u_z , where u_y is the transverse velocity and u_z is the longitudinal velocity of the electron when it reaches at a far distance from the phase shifter. For high energy electron beam (equal to 200 keV), u_z ($\gg u_y$) is determined by the beam energy. Within the paraxial approximation, u_y is calculated as in Refs. 16, 42, 43

$$u_y \approx \frac{e}{\gamma m_0 u_z} \int_{-\infty}^{\infty} dz F_y(z), \quad (2)$$

where e is the elementary charge, m_0 is the electron rest mass, and γm_0 is the relativistic electron mass ($\gamma = 1.4$ for 200 keV beam energy). $F_y(z)$ is the transverse electric field along the beam trajectory, that is given by the finite element simulation. In the simulation, u_y increases as the calculated propagation distance is extended. In the simulation below (Fig. 5), we

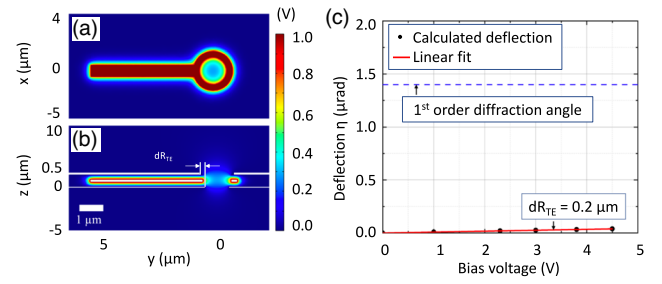


Fig. 5. (a), (b) Calculated 3D electrostatic potential of a single PE at 1 V attached with a $0.25 \mu\text{m}$ wide and 100 nm thick contact strip elongated in the y -direction, showing the potential along $z = 0.3 \mu\text{m}$. The length was set to $5 \mu\text{m}$, beyond which the unscreened contacting wire does not influence the deflection in the MIM structure for 200 keV electrons.¹⁶ (c) Transverse deflection angles calculated for 200 keV electron energy for voltages between 1 and 4.5 V in comparison to the 1st order diffraction angle to visualize how negligible deflection is for MIMIM device structure considered in the simulation .

considered the length of the CW to be long enough to reflect the modulation in u_y .

Figure 5(b) shows that the potential of the ring electrode is confined within the phase shifter cavity. From the simulation results and the above equation, the transverse deflection angle, η_s for the MIMIM structure can be calculated to $0.01 \mu\text{rad V}^{-1}$, in contrast to $0.28 \mu\text{rad V}^{-1}$ for the MIM structure in theory ($0.35 \mu\text{rad V}^{-1}$ in practice).¹⁶

2.2. Fabrication method of Boersch phase shifter device with MIMIM structure

Following the simulation results, we fabricated a three-element Boersch phase shifter device with MIMIM structure with the device parameters as described in Fig. 3. In particular, we choose a value for dR_{TE} equal to $0.2 \mu\text{m}$.⁴² The metal layers are shown in dark red, and insulator 1 and insulator 2 are shown in light gray and dark gray, respectively. The top view shows the three phase shifter elements (PE1, PE2 and PE3) in triangular arrangement. The cross-section is through the centre of PE1 parallel to the horizontal axis. The staircase-like structure shows increasing radius of the apertures from bottom to top layers. R_{BE} = the aperture radius at bottom metal and insulator 1, R_{CE} = the inner radius at central metal and insulator 2 layer, being larger than R_{BE} by 100 nm . $W_{RE} = 250 \text{ nm}$ is the width of the central ring electrode. The central ring electrode layer is 100 nm thick. The inner radius of the top electrode circle (can be seen as the big circle in Fig. 7, center image in the right panel) is equal to $R_{BE} + dR_{TE}$. The thicknesses of the central and the top metal layers are $0.1 \mu\text{m}$. The bottom metal layer thickness is 50 nm .

The device was fabricated on a low-stress SiN membrane with a thickness of 200 nm , suspended on a $250 \mu\text{m}$ thick Si frame. The diameter of the apertures was $1 \mu\text{m}$ and the separation between their centers was $1.8 \mu\text{m}$. Fabrication started with the production of a three-element device with an MIM structure.¹⁶ Briefly, on a $150 \mu\text{m}$ square suspended SiN membrane on a silicon substrate coated with Cr on the backside, apertures through the SiN and Cr are patterned by electronbeam lithography using Vistec EBPG5000 with a PMMA (600 nm thick, 950 kDa) mask and an inductively coupled plasma (ICP) reactive ion etcher with CHF_3 and Ar mixture. This was followed by patterning of Au ring

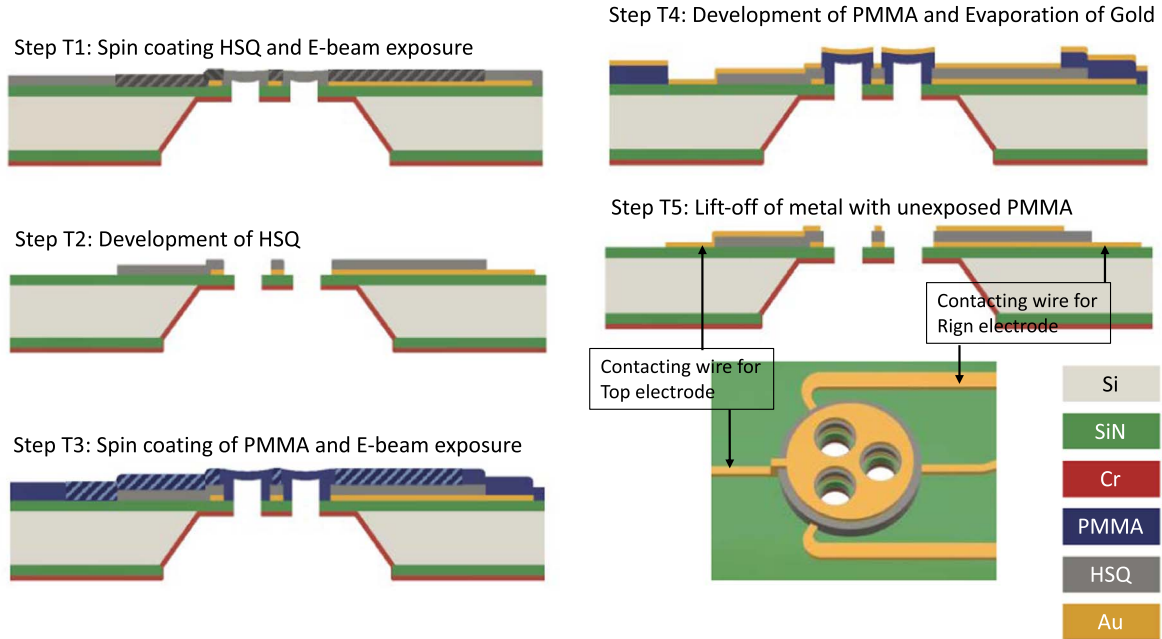


Fig. 6. Cross-sectional views of fabrication steps of MIMIM device following the fabrication of MIM structure device. Schematic Perspective view of the completed device is shown at the right bottom.

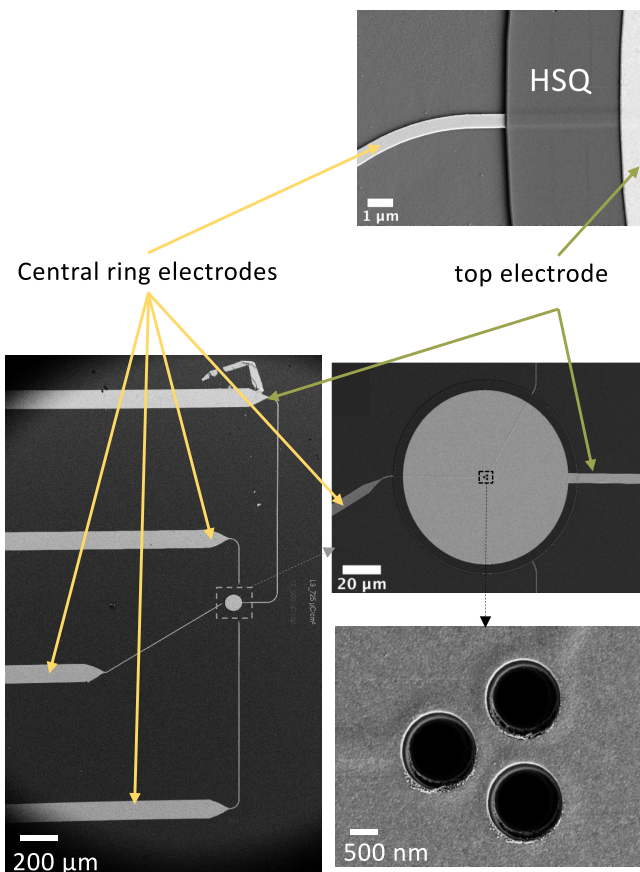


Fig. 7. The SEM micrograph of the completed three-element Boersch phase shifter with five-layer, MIMIM structure. The contact wires for the ring electrodes are screened by the top electrode above the insulator 1.

electrode (100 nm thick) by the electronbeam lithography and lift-off. An offset of 80 nm was taken between the edge of the apertures and the inner circumference of the ring electrodes.

On top of the three-layer structure, we fabricated insulator 2 and the top metal layer following the steps T1–T5 shown in Fig. 6. Insulator 2 was a cross-linked 200 nm thick hydrogen

silsesquioxane (HSQ). Insulator 2 was deposited by spin coating, and patterned by selective electron beam exposure, and development. This was followed by electron beam evaporation of the Au top electrode followed by lift-off. The top-electrode was fabricated from a 100 nm thick Au layer on the top. During Au evaporation, the resist disk of 0.2 μm was left on the apertures to protect the sidewalls and prevent an electrical short between top and the central metal layers. For this purpose, we chose a non-zero value of dR_{TE} . In addition to Figs. 1(b) and 1(c), we show in Fig. 7 the SEM images of a completed device. CWs of the ring electrodes are shielded by the top electrodes above the insulator 2 fabricated with HSQ. CWs are extended to wider contact wires connecting central ring electrodes and top electrode to the contact pads (not shown) on the far left of the bottom left image for mounting the device.

3. Experimental characterization of MIMIM phase shifter device

The phase shift performance of the device was tested in a TEM (FEI Tecnai G2 F20) using a beam energy of 200 keV. The sample was mounted on a sample holder (DENSsolutions SH30). The strength of the objective lens was reduced for recording images in far-field diffraction mode.

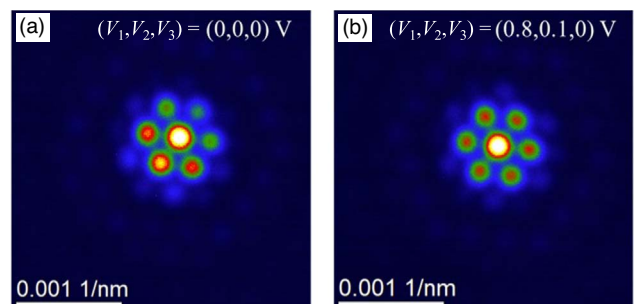


Fig. 8. Low-angle diffraction images (a) without and (b) with compensation voltages for the zero phase condition.

© 2024 The Japan Society of Applied Physics. All rights, including for text and data mining, AI training, and similar technologies, are reserved.

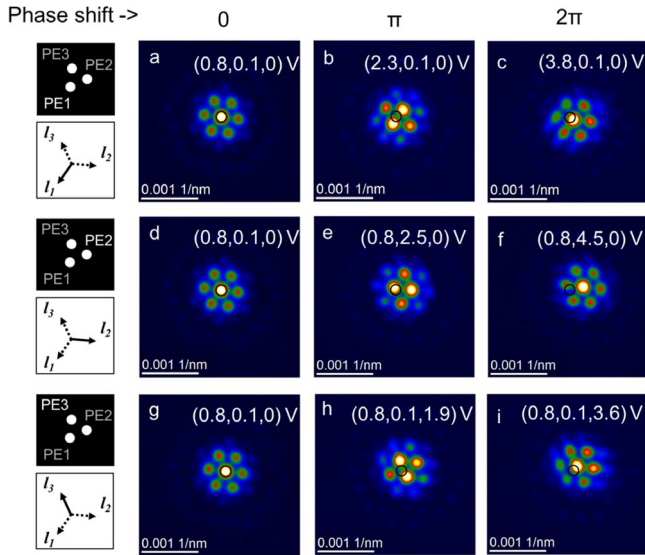


Fig. 9. Voltage-controlled three beam interference of electrons. Transmission of a coherent 200 keV electron beam through the fabricated five-element Boersch phase shifter device is imaged in the far-field diffraction setting of the microscope. (a)–(c) are for voltages V_1 applied to phase shifter element 1 (PE1) of 0.8, 2.3 and 3.8 V respectively, while the voltages applied to PE2 and PE3 were 0.1 and 0 V respectively to compensate for offset voltages for both elements. (d)–(f) and (g)–(i) show the effect of voltage variation of PE2 and PE3 respectively, for 0, π and 2π phase shifts with compensation voltages on adjacent elements. The images were captured for an instant change (within the capability of the user) of the voltages from the 2π to zero phase conditions, in order to avoid possible influence from the microscope lenses. The black circle in the center is used as a reference to highlight deflection of the image compared to the 0 phase conditions in (a), (d) and (e).

Figure 8(a) shows a recorded hexagonal interference pattern with the bias voltages to the phase shifters set to zero. Some asymmetry is present due to an offset bias of unknown origin. A symmetrical pattern with a bright central spot was obtained by compensating this offset by applying bias voltages to the phase shifters of $(V_1, V_2, V_3) = (0.8, 0.1, 0)$ V, as shown in Fig. 8(b). This offset is constant and doesn't change during the experiment as can be seen in the Fig. 9(a),(d) and (g). This offset voltage is less of a concern for a device with an array of phase shifters. Parasitic shift of the whole interference pattern was negligible, as a result of the MIMIM structure shielding the potential of the CWs by the top electrode.

Figure 9 shows interference patterns with the individual phase shifters biased for 0, π , and 2π phase shifts. For PE1, the observed phase shift was $0.67\pi \text{ rad V}^{-1}$, which is 20% lower than the phase shift achieved with the MIM structure, suggesting that the top electrode confined the potential within the ring electrode and reduced the integrated potential for five-layer device, as predicted in the simulation shown in Fig. 4(a). The observed phase shift was slightly smaller for PE2 and PE3, equal to $(0.46 \pm 0.04)\pi$ and $(0.56 \pm 0.03)\pi \text{ rad V}^{-1}$, respectively which can be a result of the minor differences in the geometry arising from the fabrication defects.

In Fig. 9, the position of the central bright spot for a zero phase shift condition is marked by a black circle. When a π -shift voltage is applied to PE1, the deflection of the interference pattern in the direction of the contact wire is $0.056 \mu\text{rad V}^{-1}$. This is 10 times smaller in comparison to the

deflection observed for the MIM structure with an unshielded CW, demonstrating the effectiveness of the MIMIM structure for reducing parasitic beam deflection. Interestingly, in contrast to the unshielded case, the deflection of the interference pattern is observed to shift predominantly in a direction other than that of the CW. For PE1 the direction of the contact wire is given by the l_1 direction from the center of the phase shifters towards the center of PE1 (marked in the insets at the left side of Fig. 9). This result suggests that the observed beam deflection is caused by another mechanism (e.g. the contact to the sample holder). Similarly, the deflection for PE3 is also observed mostly in the l_1 -direction and not in the l_3 -direction, i.e. unrelated to the direction of the contact wire. Contrary, small deflection of $0.25 \mu\text{rad V}^{-1}$ is observed for PE2 in the l_2 -direction.

The origin of the variation in phase shift with applied voltage between the apertures (of $\sim 20\%$) is unclear. The phase shift is expected to be proportional to the spatial integration of the potential in the beam direction, suggesting that a difference may arise from a variation in ring-electrode thickness T_{RE} , top-electrode aperture size or dR_{TE} . High-resolution SEM inspection does not indicate a difference in the value of T_{RE} (nominally 100 nm) of ~ 20 nm. Referring to the calculated phase shift as a function of dR_{TE} [Fig. 4(b)], the lithographic precision of ~ 50 nm (in size and alignment) in the value of dR_{TE} of $0.2 \mu\text{m}$ is too small to explain the observed phase shift variation of $\sim 20\%$. Further research is needed to determine the origin of this variation and to improve the uniformity of phase shifter performance.

4. Summary and discussion

In summary, we have demonstrated the fabrication of a three-element Boersch phase shifter device using a CMOS-compatible method. By adopting an MIMIM structure, we demonstrated minimal parasitic beam deflection and cross-talk. These are important for applications in programmable phase shifter arrays with large number of phase shifter elements. The fabricated device shows a π -shift for a voltage swing of (2.10 ± 0.28) V for a 200 keV coherent electron beam. Further research is under way in the scientific community on the design and fabrication of multi-element phase shifter arrays for applications in electron beam shaping, imaging, aberration correction, massively parallel electron beam lithography and the production of arbitrary electron wave fronts.

An important next step is the realization of increased number of PEs. The fabrication of devices with increased numbers of PEs from 3 to ~ 10 appears to be straightforward, e.g. in circular or hexagonal arrangements for producing vortex beams with the method presented in this work. In contrast to the use of a static holographic mask to produce a vortex beam in a high order diffraction direction, a phase shifter array can be used to produce a vortex beam in the direct beam direction with higher efficiency. Although the offset voltage and phase shift as a function of applied bias have to be known for such applications. Their calibration is straightforward, e.g. by determining the voltages that result in a symmetrical interference pattern during characterization of the device. The fabrication of devices with even larger number of PEs e.g. 10^2 – 10^4 elements promises to be of practical significance for applications such as the correction of spherical aberration.¹⁴⁾ Their production is likely to require

a different design of electrical contacts to the individual phase shifters. Solutions adopted for memory devices, such as matrix connections via horizontal and vertical wiring with switching elements at each node (corresponding to a phase element in the present case), requires radiation tolerance of the switches. Although radiation could result in breakdown for standard MOSFET switches,⁴⁴⁾ memristors have recently been studied as potential radiation-tolerant switches.^{45,46)} Alternatively (in particular for smaller arrays), direct wiring to each of the phase elements is a possibility.⁴⁷⁾ In order to minimize space between phase shifters for increasing beam transmission per unit area, a multi-layer design may be needed, together with strain control in the fabrication steps. Although it is desirable to eliminate the phase shift variation and offset voltage, it is feasible to calibrate these effects, e.g. via parametric optimization for producing a minimal focal size, since the phase distribution can then be identified as that created by an ideal lens. Nevertheless, we note that such design considerations and fabrication strategy is closely related to the phase shifter functions and performance targeted for the device. For example, as is well known for the optical phase shifter arrays, one should avoid the regular array arrangement to avoid the grating effect.⁴⁸⁾ The development of a wiring design strategy and fabrication steps are subjects for future study.

Acknowledgments

The authors extend their sincere thanks to Prof. Giulio Pozzi (University of Bologna, Italy) for his insight and motivation for this work. They also thank the Laboratory of Micro- and Nanotechnology (LMN) in the Paul Scherrer Institut (PSI) for support and excellent clean room laboratory infrastructure for device fabrication, as well as Jana Lehmann (LMN, PSI) for help with silicon nitride membrane fabrication. This work was funded by the Swiss Nanoscience Institute Nr. 1505.

Author contributions

S.T. and J.P.A. conceived the experiment. P.T. conducted the FEM simulation and fabricated the device. V.G. and S.T. supported the simulation and fabrication. P.-H.L. conducted the TEM experiment under the supervision of R.D.-B. and in close communication with P.T. and S.T. P.T. and S.T. analyzed the data and wrote the manuscript. All of the authors read the manuscript and agreed to the contents.

ORCID iDs

Soichiro Tsujino  <https://orcid.org/0000-0001-7401-7815>

- 1) R. Shiloh, Y. Lereah, Y. Lilach, and A. Arie, *Ultramicroscopy* **144**, 26 (2014).
- 2) R. Shiloh and A. Arie, *Ultramicroscopy* **177**, 30 (2017).
- 3) D. Roitman, R. Shiloh, P.-H. Lu, R. E. Dunin-Borkowski, and A. Arie, *ACS Photonics* **8**, 3394 (2021).
- 4) M. Uchida and A. Tonomura, *Nature* **464**, 737 (2010).
- 5) J. Verbeeck, H. Tian, and P. Schattschneider, *Nature* **467**, 301 (2010).
- 6) B. J. McMorran, A. Agrawal, I. M. Anderson, A. A. Herzing, H. J. Lezec, J. J. McClelland, and J. Unguris, *Science* **331**, 192 (2011).
- 7) V. Grillo, G. C. Gazzadi, E. Karimi, E. Mafakheri, R. W. Boyd, and S. Frabboni, *Appl. Phys. Lett.* **104**, 043109 (2014).
- 8) N. Voloch-Bloch, Y. Lereah, Y. Lilach, A. Gover, and A. Arie, *Nature* **494**, 331 (2013).
- 9) V. Grillo, E. Karimi, G. C. Gazzadi, S. Frabboni, M. R. Dennis, and R. W. Boyd, *Phys. Rev. X* **4**, 011013 (2014).
- 10) V. Grillo, J. Harris, G. C. Gazzadi, R. Balboni, E. Mafakheri, M. R. Dennis, S. Frabboni, R. W. Boyd, and E. Karimi, *Ultramicroscopy* **166**, 48 (2016).
- 11) G. D. Love, *Appl. Opt.* **36**, 1517 (1997).
- 12) A. H. Tavabi, V. Migunov, C. Dwyer, R. E. Dunin-Borkowski, and G. Pozzi, *Ultramicroscopy* **157**, 57 (2015).
- 13) G. Pozzi, P.-H. Lu, A. H. Tavabi, M. Duchamp, and R. E. Dunin-Borkowski, *Ultramicroscopy* **181**, 191 (2017).
- 14) J. Verbeeck, A. Béché, K. Müller-Caspary, G. Guzzinati, M. A. Luong, and M. Den Hertog, *Ultramicroscopy* **190**, 58 (2018).
- 15) A. H. Tavabi, H. Larocque, P.-H. Lu, M. Duchamp, V. Grillo, E. Karimi, R. E. Dunin-Borkowski, and G. Pozzi, *Phys. Rev. Res.* **2**, 13185 (2020).
- 16) P. Thakkar, V. A. Guzenko, P.-H. Lu, R. E. Dunin-Borkowski, J. P. Abrahams, and S. Tsujino, *J. Appl. Phys.* **128**, 134502 (2020).
- 17) F. Zernike, *Physica* **9**, 686 (1942).
- 18) T. Latychevskaja and H.-W. Fink, *Phys. Rev. Lett.* **98**, 233901 (2007).
- 19) Z. Chen, Y. Jiang, Y.-T. Shan, M. E. Holtz, M. Odstroil, M. Guizar-Sicairos, I. Hanke, S. Ganshow, D. G. Schom, and D. A. Muller, *Science* **372**, 826 (2021).
- 20) H. Ochner, S. Szilagyí, M. Edte, L. Malavolti, S. Rauschenbach, and K. Kern, *ACS Nano* **16**, 18658 (2022).
- 21) R. Danev and K. Nagayama, *J. Phys. Soc. Jpn.* **v70**, 696 (2001).
- 22) H. Müller, J. Jin, R. Danev, J. Spence, H. Padmore, and R. M. Glaeser, *New J. Phys.* **12**, 073011 (2010).
- 23) R. Danev and W. Baumeister, *eLife* **5**, e13046 (2016).
- 24) K. Schultheiss, F. Perez-Willard, B. Barton, D. Gerthsen, and R. Schröder, *Rev. Sci. Instrum.* **77**, 33701 (2006).
- 25) E. Majorovits, B. Barton, K. Schultheiß, F. Pérez-Willard, D. Gerthsen, and R. Schröder, *Ultramicroscopy* **107**, 213 (2007).
- 26) R. Cambie, K. H. Downing, D. Typke, R. M. Glaeser, and J. Jin, *Ultramicroscopy* **107**, 329 (2007).
- 27) J. Shiue et al., *J. Electron Microsc.* **58**, 137 (2009).
- 28) M. P. Edgar, G. M. Gibson, and M. J. Padgett, *Nat. Photonics* **13**, 13 (2019).
- 29) A. Kallepalli et al., *Intelligent Computing* **2022**, 0001 (2022).
- 30) A. Konečná, E. Rotunno, V. Grillo, F. J. García de Abajo, and G. M. Vanacore, *ACS Photonics* **10**, 1463 (2023).
- 31) M. Kozák, T. Eckstein, N. Schönenberger, and P. Hommelhoff, *Nat. Phys.* **14**, 121 (2018).
- 32) O. Schwartz, J. J. Axelrod, S. L. Campbell, C. Tumbaugh, R. M. Glaeser, and H. Müller, *Nat. Methods* **16**, 1016 (2019).
- 33) O. Kfir, V. Di Giulio, F. J.-G. de Abajo, and C. Ropers, *Sci. Adv.* **7**, eabf6380 (2021).
- 34) M. Tsarev, A. Ryabov, and P. Baum, *Phys. Rev. Res.* **3**, 043033 (2021).
- 35) I. Madan et al., *ACS Photonics* **9**, 3215 (2022).
- 36) M. C.-C. Mihaila, P. Weber, M. Schneller, L. Grandits, S. Nimmrichter, and T. Juffmann, *Phys. Rev. X* **12**, 031043 (2022).
- 37) S. Tsesses, R. Dahan, K. Wang, T. Bucher, K. Cohen, O. Reinhardt, G. Bartal, and I. Kaminer, *Nat. Mater.* **22**, 345 (2023).
- 38) A. Walter et al., *Ultramicroscopy* **116**, 62 (2012).
- 39) H. Boersch, *Z. Naturforsch. A* **2**, 615 (1947).
- 40) T. Matsumoto and A. Tonomura, *Ultramicroscopy* **63**, 5 (1996).
- 41) P. Helfenstein, K. Jefimovs, E. Kirk, C. Escher, H.-W. Fink, and S. Tsujino, *J. Appl. Phys.* **112**, 093307 (2012).
- 42) P. Thakkar, "Dissertation," The outline of the present work was previously presented at 2021 34th Int. Vacuum Nanoelectronics Conf. (IVNC), Lyon, France, 2021 University of Basel (2023). P. Thakkar, V. A. Guzenko, P.-H. Lu, R. E. Dunin-Borkowski, J. P. Abrahams, and S. Tsujino, "Voltage-controlled three-electron-beam interference by a three-element Boersch phase shifter with top and bottom shielding electrodes," 2021 34th Int. Vacuum Nano-electronics Conf. (IVNC) (Lyon, France), 2021, [10.1109/IVNC52431.2021.9600711](https://doi.org/10.1109/IVNC52431.2021.9600711).
- 43) L. Reimer, *Transmission Electron Microscopy: Physics of Image Formation and Microanalysis* (Springer, Berlin, 1984).
- 44) A. Paccagnella, A. Cester, and G. Cellere, IEDM Technical Digest. IEEE Int. Electron Devices Meeting 2004, [10.1109/IEDM.2004.1419192](https://doi.org/10.1109/IEDM.2004.1419192).
- 45) Y. Wang et al., *IEEE Electron Device Lett.* **31**, 1470 (2010).
- 46) D. P. Pattnaik, C. Andrews, M. D. Cropper, A. Balanov, S. Saveliev, and P. Borisov, (2023), [arXiv:2303.12762](https://arxiv.org/abs/2303.12762).
- 47) C.-P. Yu, F. V. Ibanez, A. Besche, and J. Verbeeck, *SciPost Phys.* **15**, 223 (2023), This work reported a 48-element Boersch phase shifter array, which was published after our experiments were completed (see Ref. 42). Their device structure appeared to have adopted the direct wiring design. However, details are not clear since the authors did not report the details of the device design and fabrication processes.
- 48) C. Benoît-Pasanau, F. Goudail, P. Chavel, J.-P. Cano, and J. Ballet, *Appl. Opt.* **50**, 509 (2011).